Supporting Information

Multilayer Iontronic Sensors with Controlled Charge Gradients for High-Performance, Self-Powered Tactile Sensing

Haryeong Cho[§1], *Young-Ryul Kim*[§1], *Jaehun Kim*[§2], *Seungjae Lee*[1], *Seokhee Jung*[1], *Jeeyoon Kim*[1], *Jinyoung Kim*[1], *Yong-Jin Park*[1], *Sung-Phil Kim**[2], *Hyunhyub Ko**[1]

[1]School of Energy and Chemical Engineering, Ulsan National Institute of Science and Technology (UNIST), Ulsan Metropolitan City, 44919, Republic of Korea

[2]College of Information-Bioconvergence Engineering, Department of Biomedical Engineering, Ulsan National Institute of Science and Technology (UNIST), Ulsan Metropolitan City, 44919, Republic of Korea

*Corresponding Author E-mail: hyunhko@unist.ac.kr

[§]These authors are equally contributed.

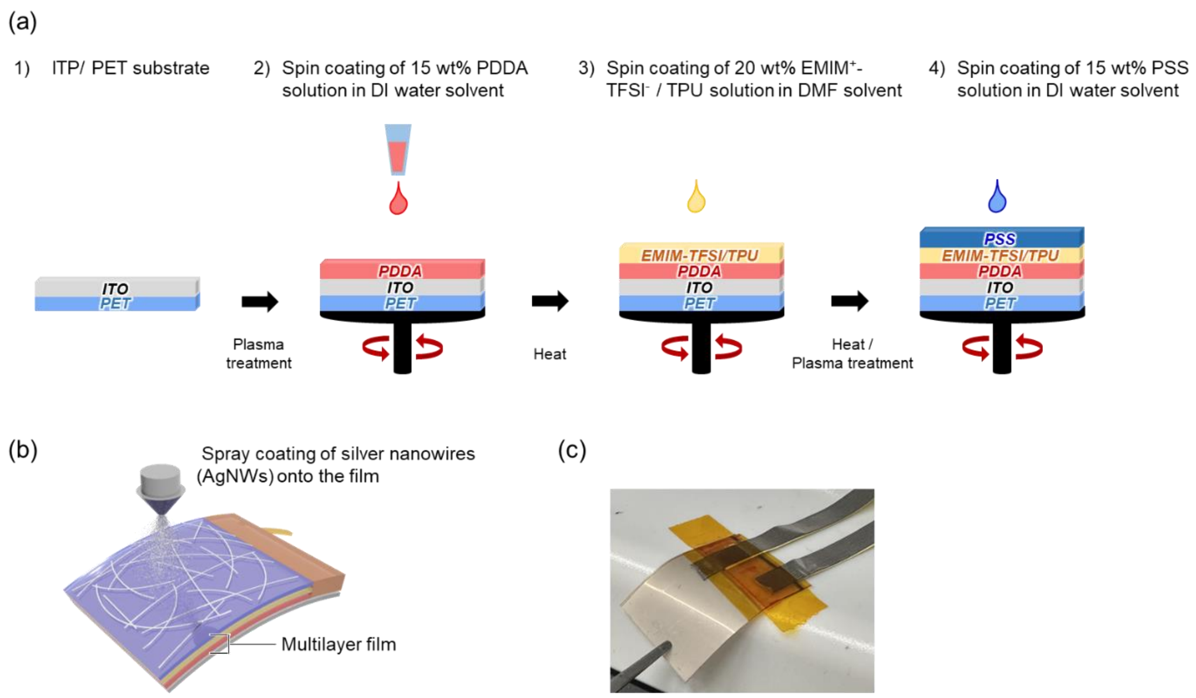

Figure S1. . (a)Schematic illustration of fabrication process of multilayered iontronic tactile sensor. (b) Schematic illustration of spray coating process of silver nanowires (AgNWs) onto the multilayer film to create flexible electrodes (c) Optical images corresponding to the fabricated sensor (sensor size showing 2 x 2 cm^2)

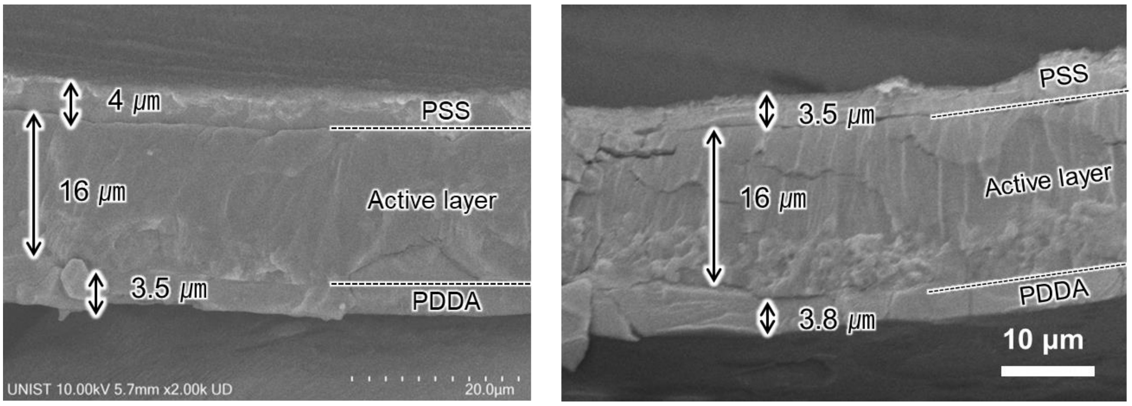

Figure S2. Scanning electron microscopy (SEM) cross-sectional images showing the layered structure of the iontronic tactile sensor. The total thickness of approximately 24 μm consists of a PSS layer (3.5-4 μm), an active layer (16 μm), and a PDDA layer (3.5-3.8 μm).

(a)

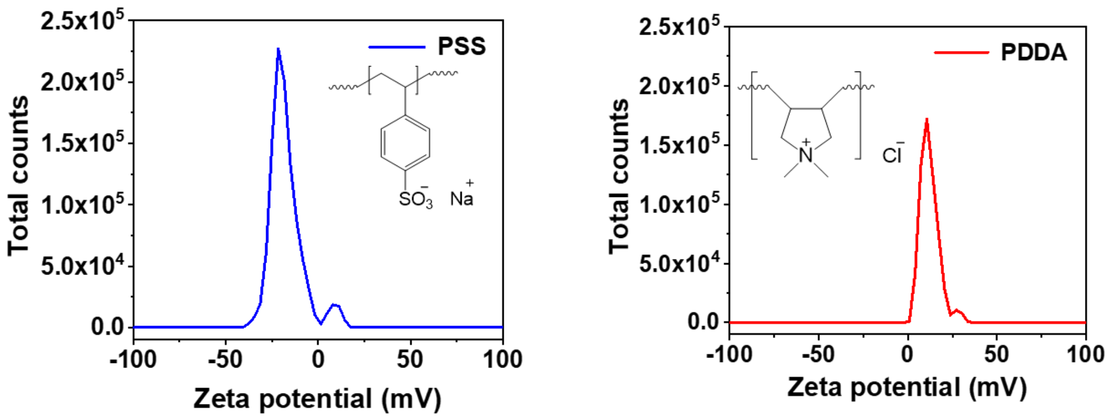

(b)

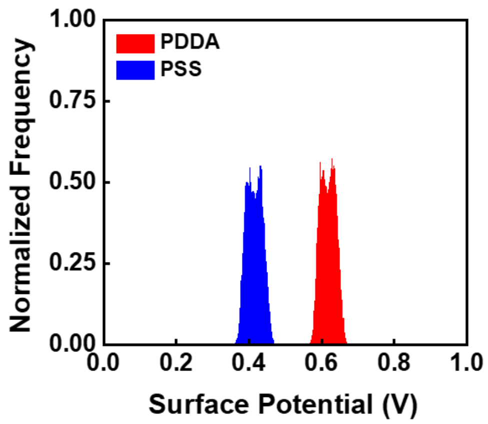

Figure S3. Chemical and electrical characterization of polyelectrolytes. (a) Chemical structures of PSS and PDDA showing their pendant ionic groups, with measured zeta potential values of -10.6 mV for PSS and 18.6 mV for PDDA in DI water. (b) Surface potential difference ($V_{CPD} = {\emptyset_{Tip} - \emptyset_{sample}}/{-e}$) of PSS and PDDA solid films shows the contact potential difference for each film relative to a reference tip. The histogram reveals distinct potential distributions with PSS exhibiting lower surface potential (centered around 0.4 V) and PDDA showing higher surface potential (centered around 0.6 V), confirming the negative and positive charge characteristics observed in their respective solution states.

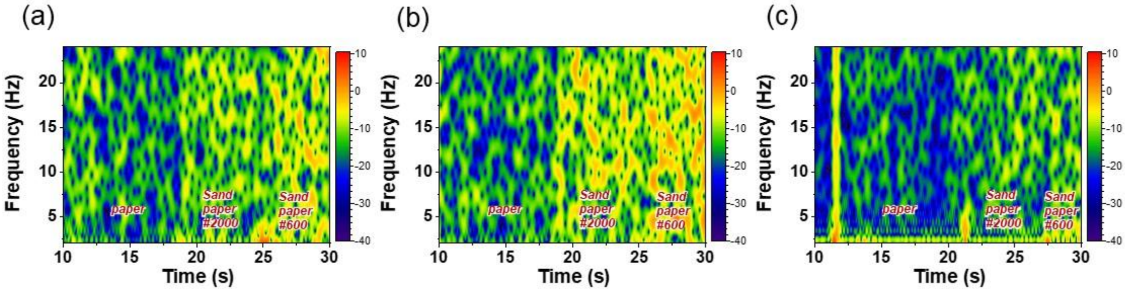

Figure S4. STFT results of surface texture sensing using sensors with different active layer thicknesses: (a) 9 μm, (b) 16 μm, and (c) 24 μm. Each sensor was tested on paper, sandpaper #2000, and sandpaper #600.

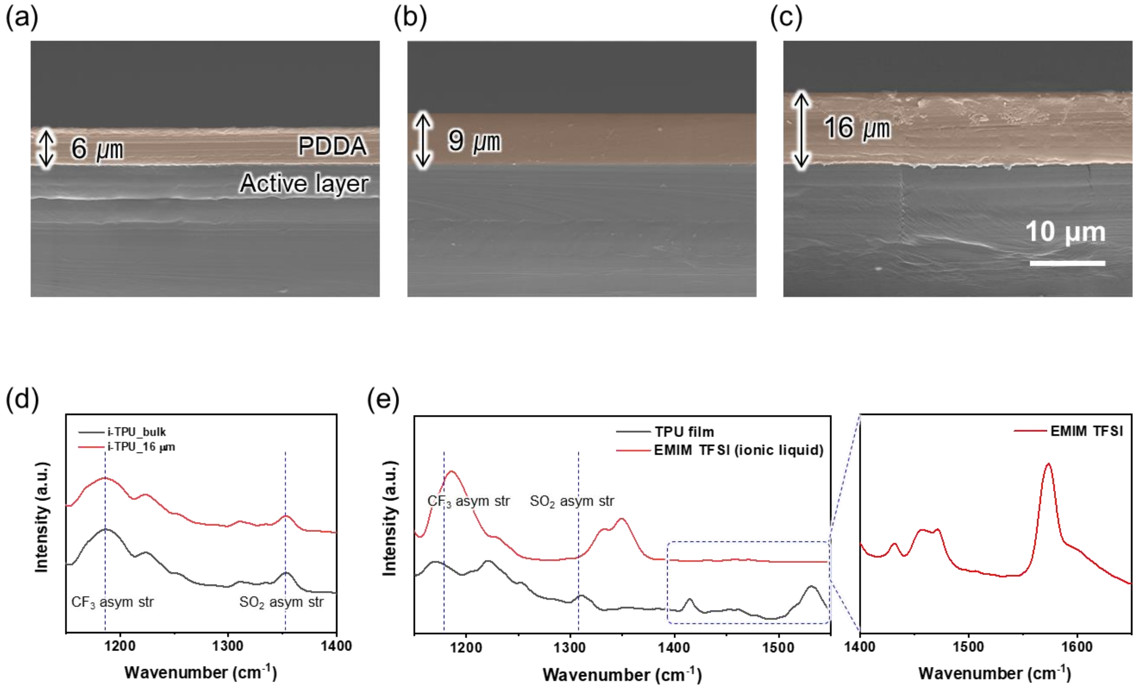

Figure S5. Analysis of ion distribution in active layers of varying thicknesses. (a-c) ATR-FTIR spectra of active layers with thicknesses of 6, 9, and 16 μm deposited on polyelectrolytes layers. (d) Comparison of $TFSI^-$ peaks in the active layer at different distances from the PDDA surface, showing decreasing anion concentration with increasing distance. (e) Comparison o^+ peaks in the ionic liquid relative to pristine TPU film, demonstrating weaker intensities for the CF_3 asymmetric stretching and SO_2 asymmetric stretching vibrations, and detailed view of $EMIM^+$ $TFSI^-$ characteristic peaks in the 1400-1550 cm-1 region.

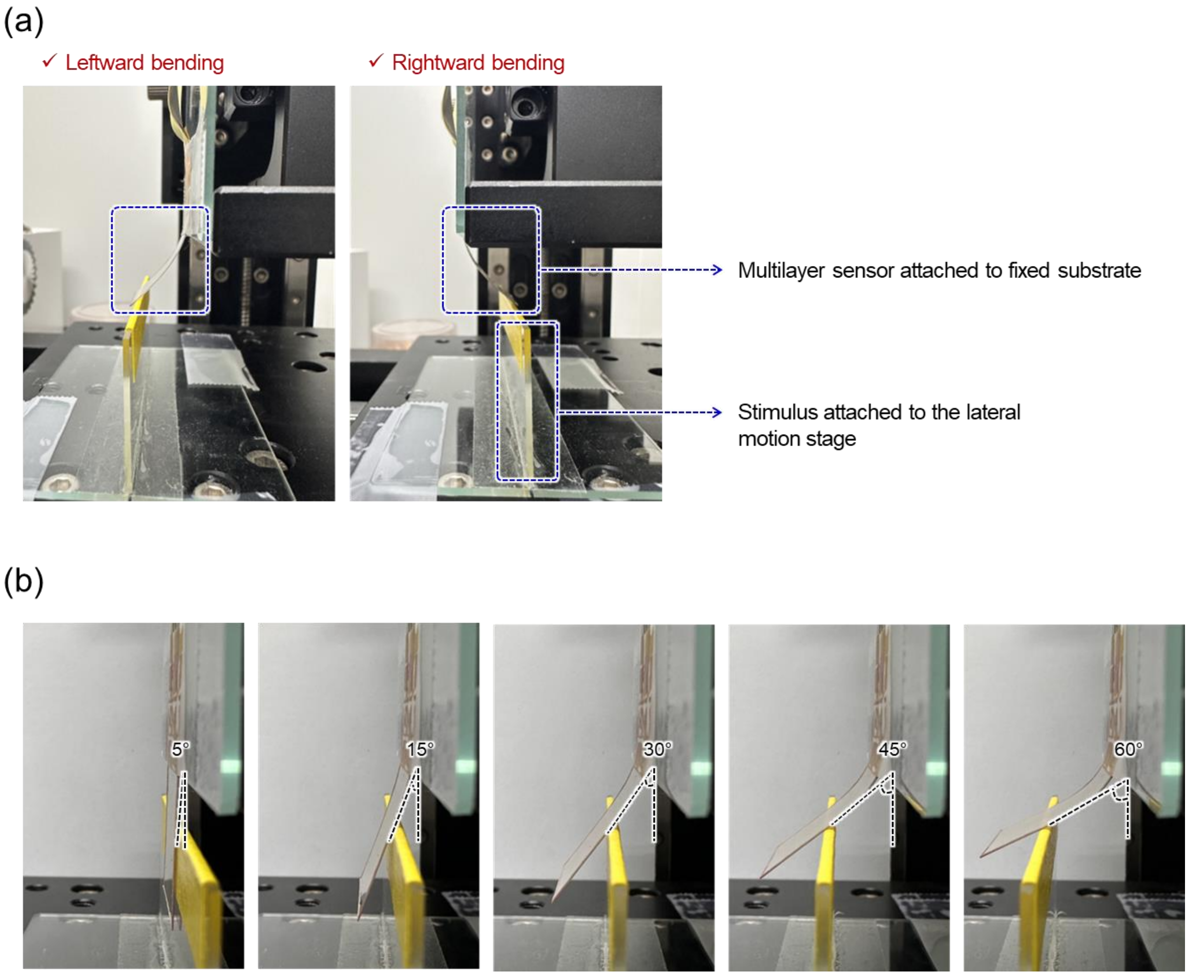

Figure S6. Experimental setup for piezoionic testing under bending conditions. (a) Optical images showing the multilayer sensor attached to a fixed substrate being bent leftward and rightward using a stimulus attached to the lateral motion stage. (b) Sequential images demonstrating increasing bending degrees of the sensor, corresponding to increasing internal stress with larger bending angles.

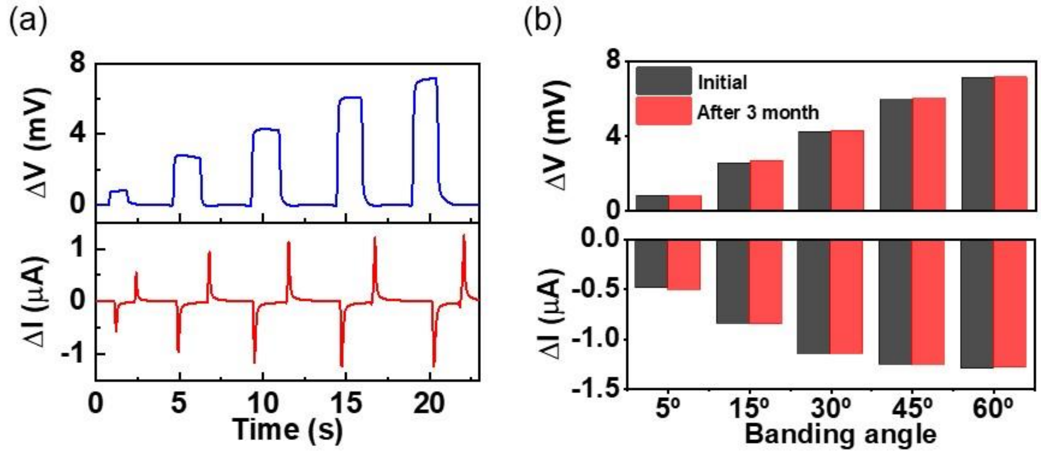

Figure S7. (a) Voltage and current responses of the multilayer sensor at various bending angles (0° to 60°) after 3 months of ambient storage without encapsulation. (b) Comparison of output amplitudes before and after storage shows minimal variation, indicating excellent long-term air stability.

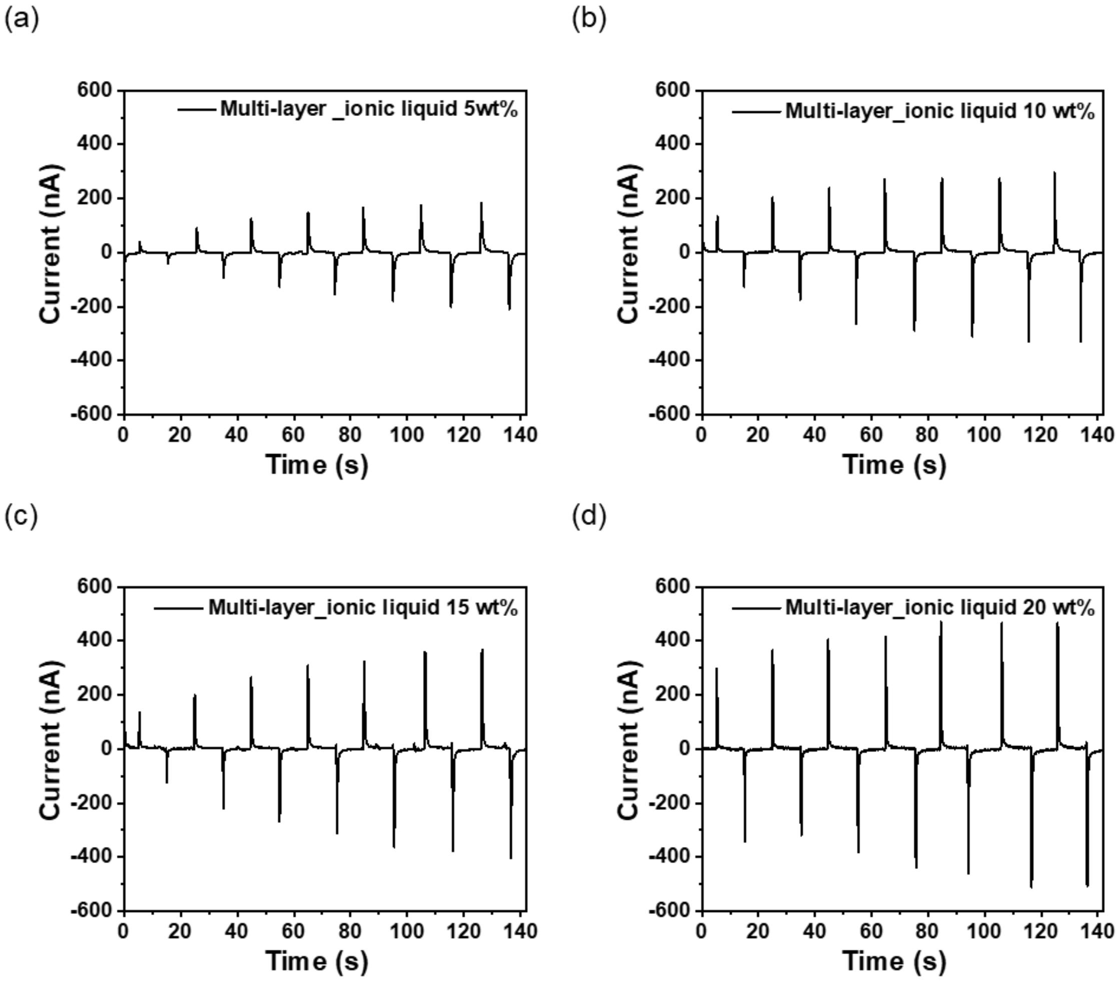

Figure S8. Effect of ionic liquid (IL) concentration on piezoionic signal generation. Time-dependent current response of the multilayer sensor with varying ionic liquid concentrations: (a) 5 wt%, (b) 10 wt%, (c) 15 wt%, and (d) 20 wt%. Higher ionic liquid content results in enhanced electrical signals due to increased segmental motion of polymer chains.

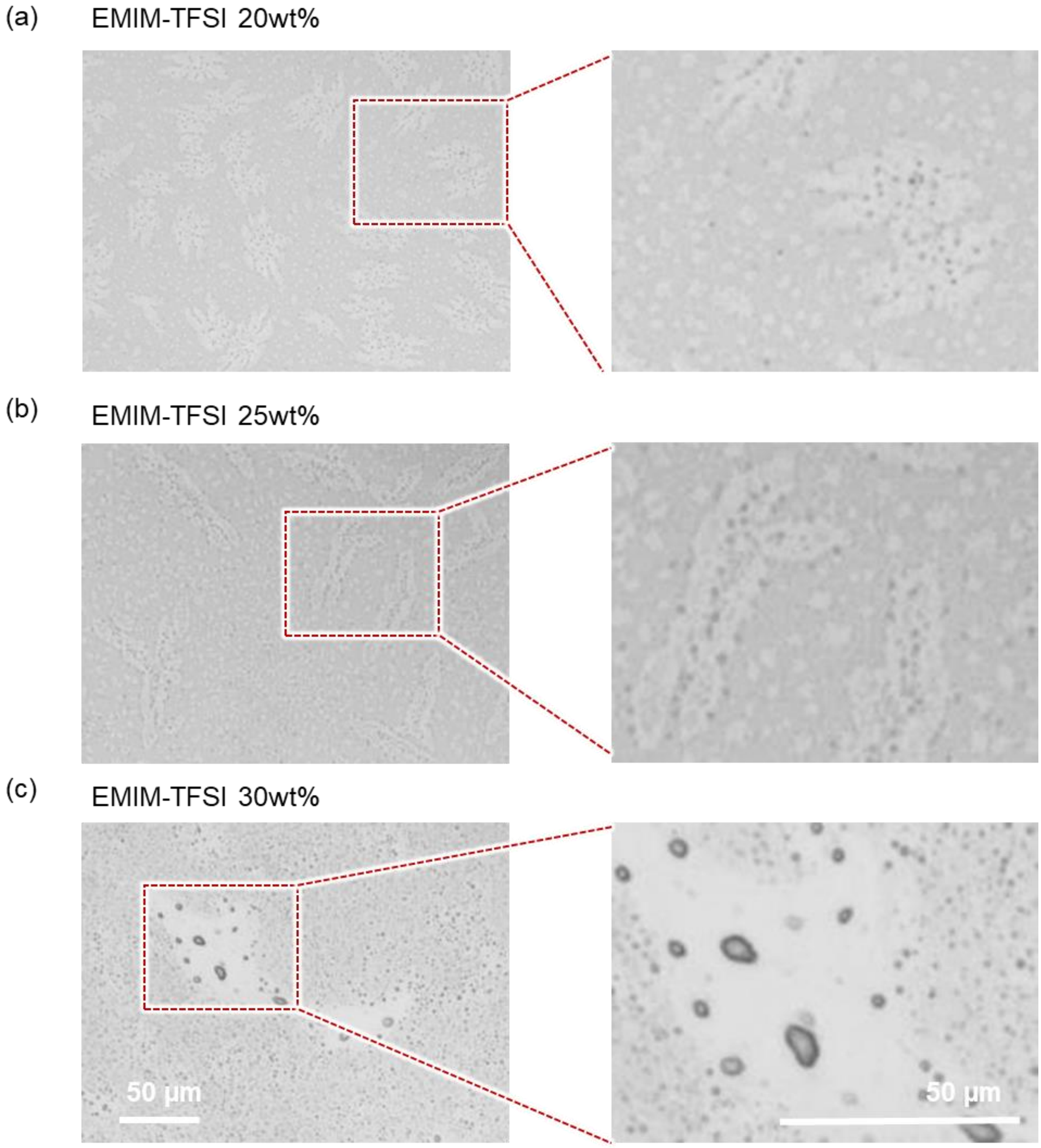

Figure S9. Optical microscope images showing the surface morphologies of TPU/$EMIM^+$-$TFSI^-$ composites with varying ionic liquid content: (a) 20 wt%, (b) 25 wt%, and (c) 30 wt% of $EMIM^+$-$TFSI^-$.

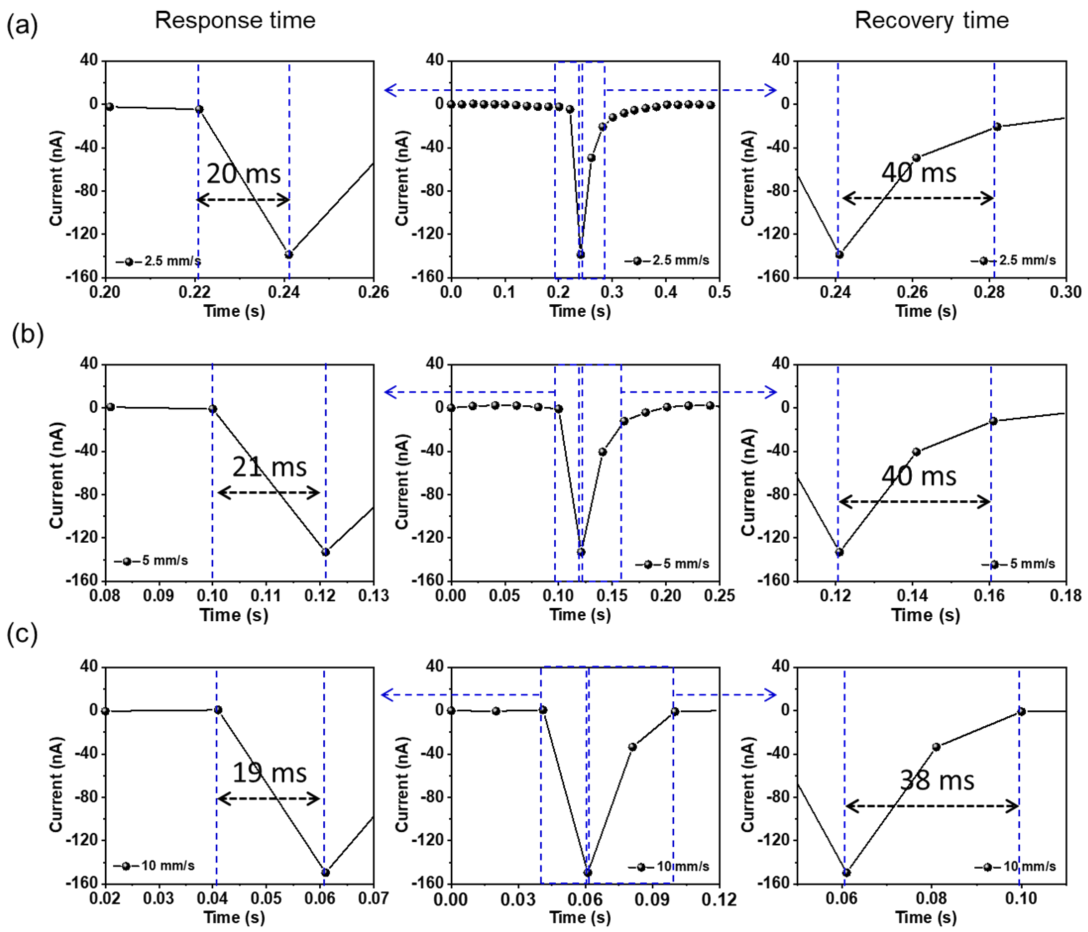

Figure S10. Piezoionic performance under bending stimulation including response and recovery time at varying measurement speeds: (a) 2.5 mm/s, (b) 5 mm/s, and (c) 10 mm/s.

(a)

	$R_{TPU/IL}$ (Ω)	$C_{TPU/IL}$ (F)	Q_{EDL} (F)	R_{P-N} (Ω)	Q_{P-N} (F)
S-layer	529.1	3.2E-10	2.3E-5	-	-
M-layer	437.9	2.5E-10	6.7E-5	5649	1.39E-5

(b)

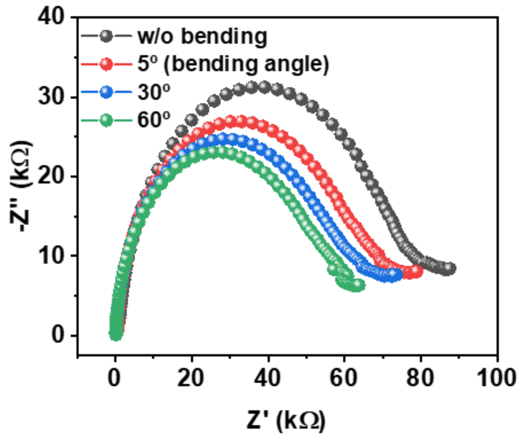

(c)

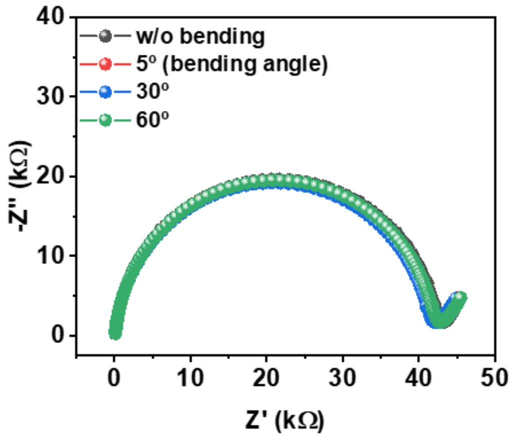

Figure S11. Electrochemical impedance spectroscopy (EIS) analysis comparing single-layer (S-layer) and multilayer (M-layer) sensors. (a) Fitted values of circuit elements including input resistance (Rinput), input capacitance (Cinput), electrical double layer capacitance (CEDL), ion resistance (Rion), and ion capacitance (Cion). (b) Nyquist plots showing impedance changes of the multilayer sensor under various bending deformations. (c) Nyquist plots of the single-layer sensor demonstrating no significant changes under identical bending conditions.

(a)

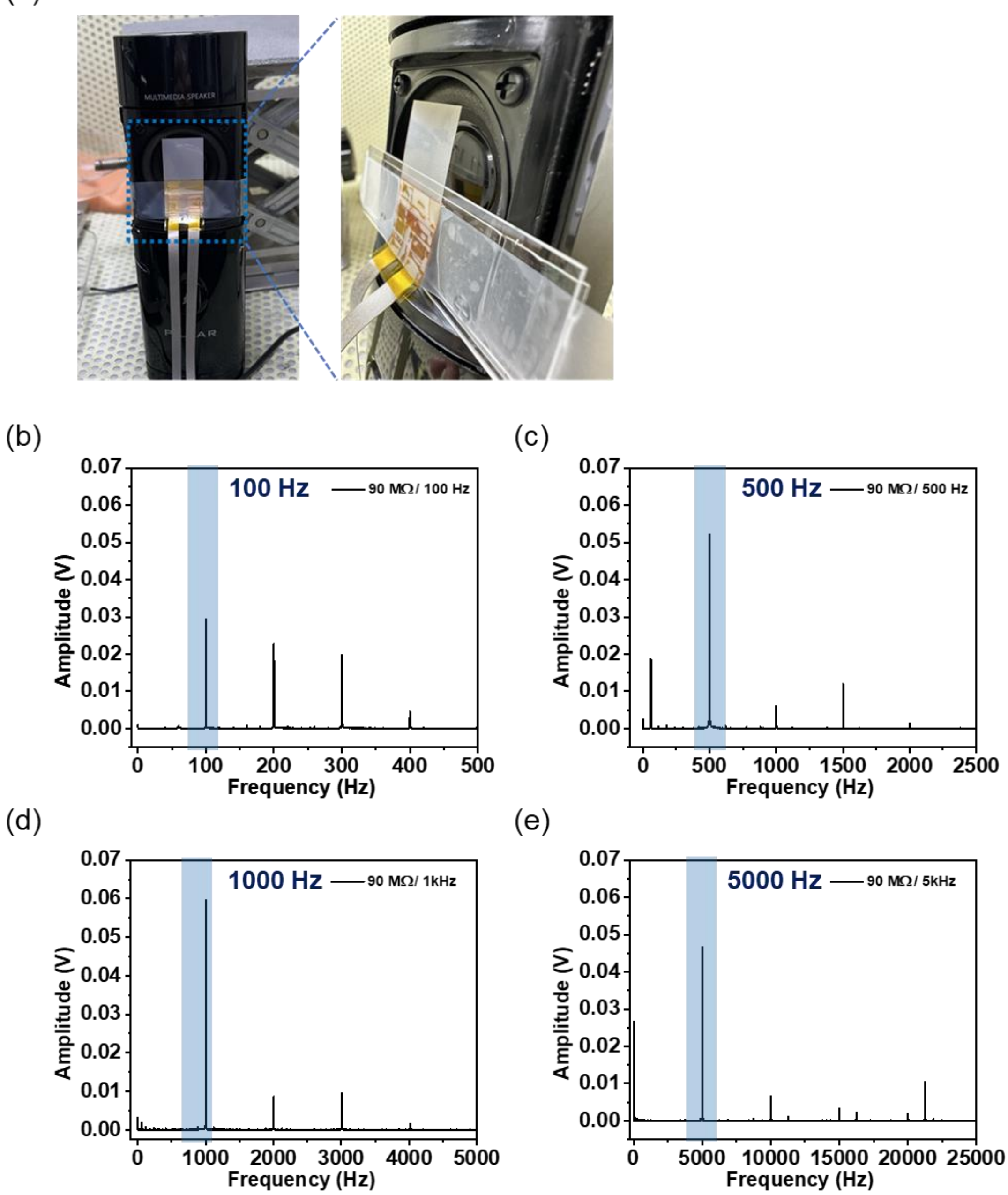

Figure S12. Sound detection capabilities of the multilayer sensor. (a) Experimental setup showing the sensor attached to a loudspeaker for acoustic testing. (b-e) Frequency domain analysis of the sensor response to various sound frequencies: (b) 100 Hz, (c) 500 Hz, (d) 1000 Hz, and (e) 5000 Hz, demonstrating the sensor's ability to accurately detect and differentiate acoustic signals across a wide frequency range.

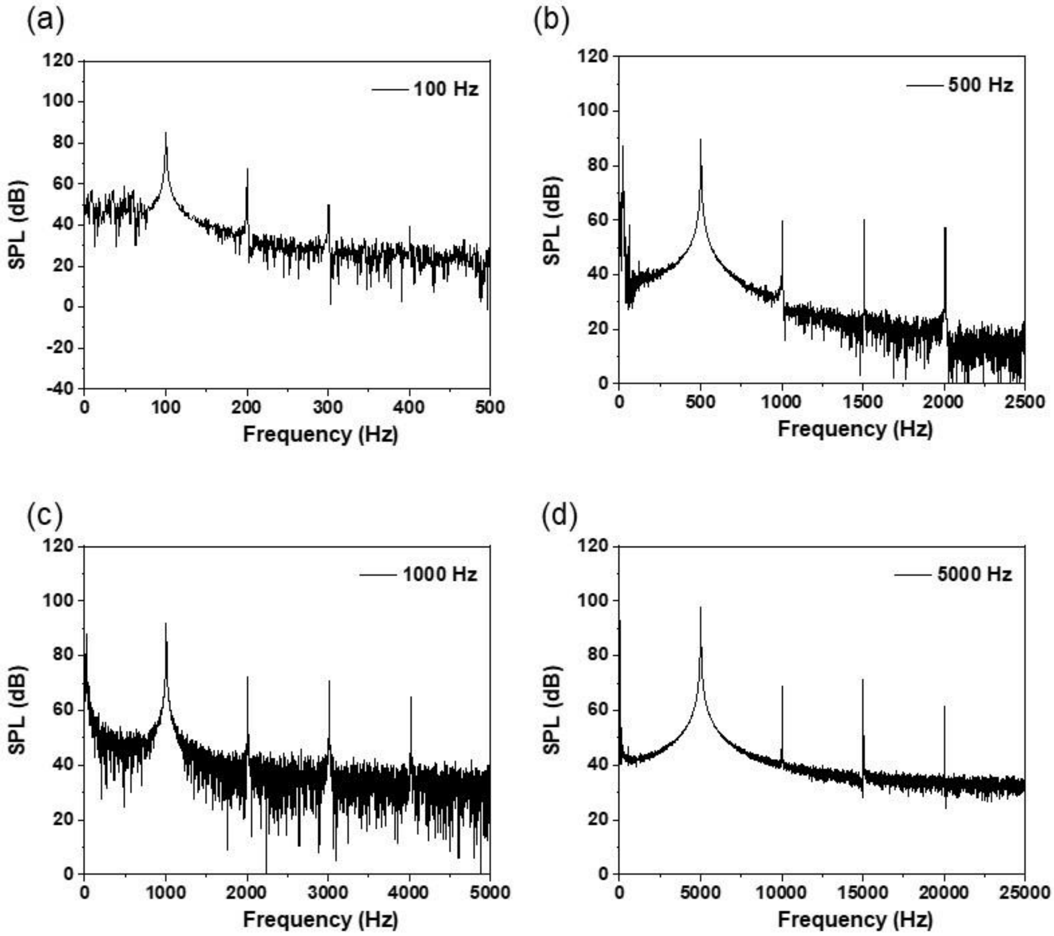

Figure S13. SPL spectra of the audio stimuli used in Supplementary Figure S12. The measured SPLs were approximately 84 dB (100 Hz), 87 dB (500 Hz), 91 dB (1000 Hz), and 98 dB (5000 Hz).

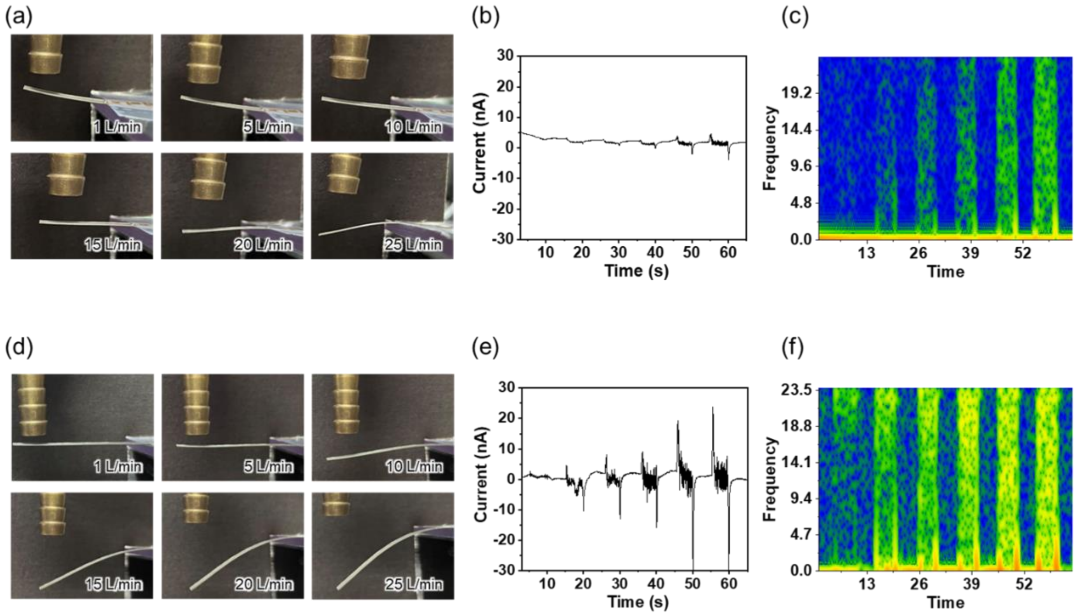

Figure S14. Aspect ratio-dependent piezoionic properties of the multilayer sensor. (a) Sequential images showing minimal bending of a lower aspect ratio sensor (1 × 2 cm² rectangular dimension) under increasing air flow rates from 1.0 L/min to 25.0 L/min. (b) Current-time response of the lower aspect ratio sensor showing minimal signal variation. (c) Short-time Fourier transform (STFT) analysis of the lower aspect ratio sensor. (d) Sequential images demonstrating significantly higher bending deformation of a higher aspect ratio sensor EMIof the higher aspect ratio sensor showing pronounced electrical signals with both instantaneous and continuous current peaks corresponding to bending and vibration. (f) STFT analysis showing increased intensity for the higher aspect ratio sensor due to greater physical stress.

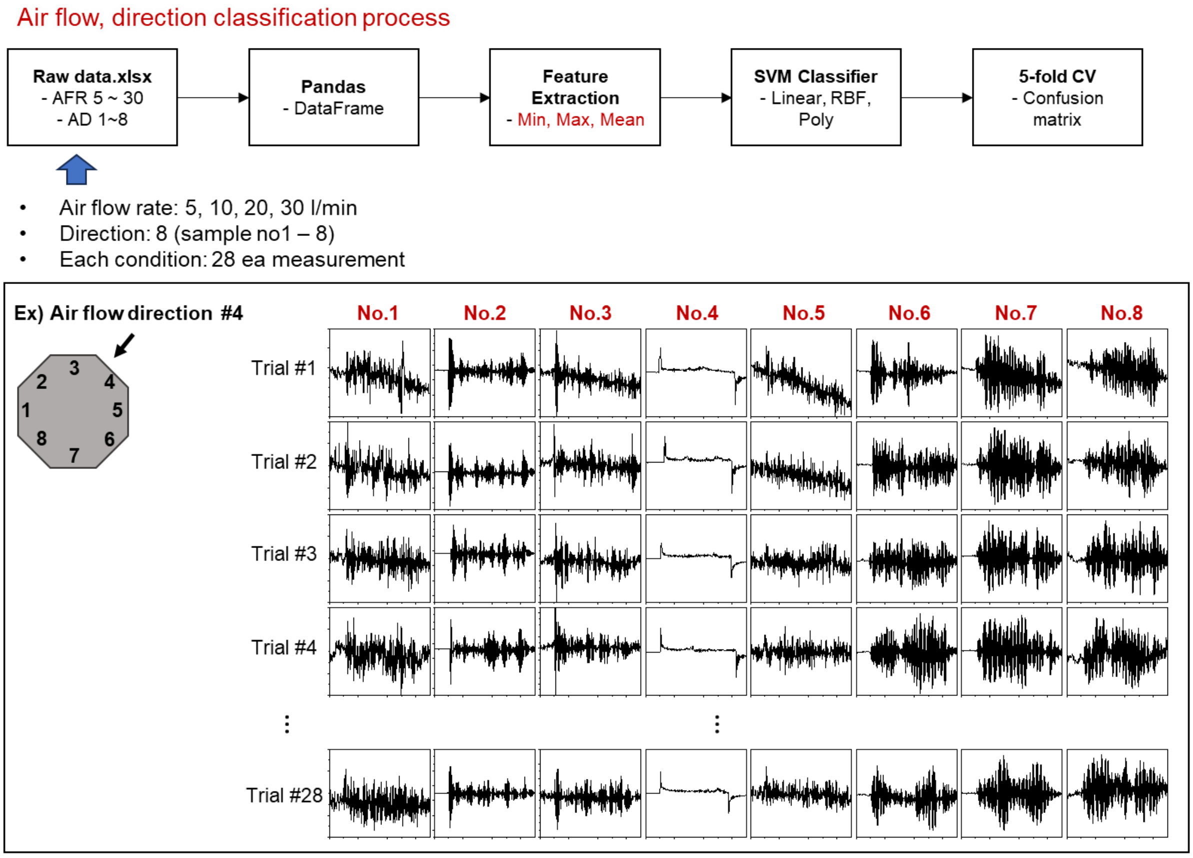

Figure S15. Machine learning framework for airflow direction classification using multiple sensor data. The top panel shows raw current signals from eight different sensors (No.1-8) positioned on an octagonal support structure, each responding to airflow from different directions (numbered 1-8). The bottom panel illustrates the data processing pipeline: raw data collected at various airflow rates (5, 10, 20, 30 L/min) with 28 measurements per condition is exported to Excel format, processed using Pandas for data frame operations, analyzed for feature extraction (minimum, maximum, mean values), classified using SVM models with different kernels (Linear, RBF, Polynomial), and evaluated through 5-fold cross-validation with confusion metrics.

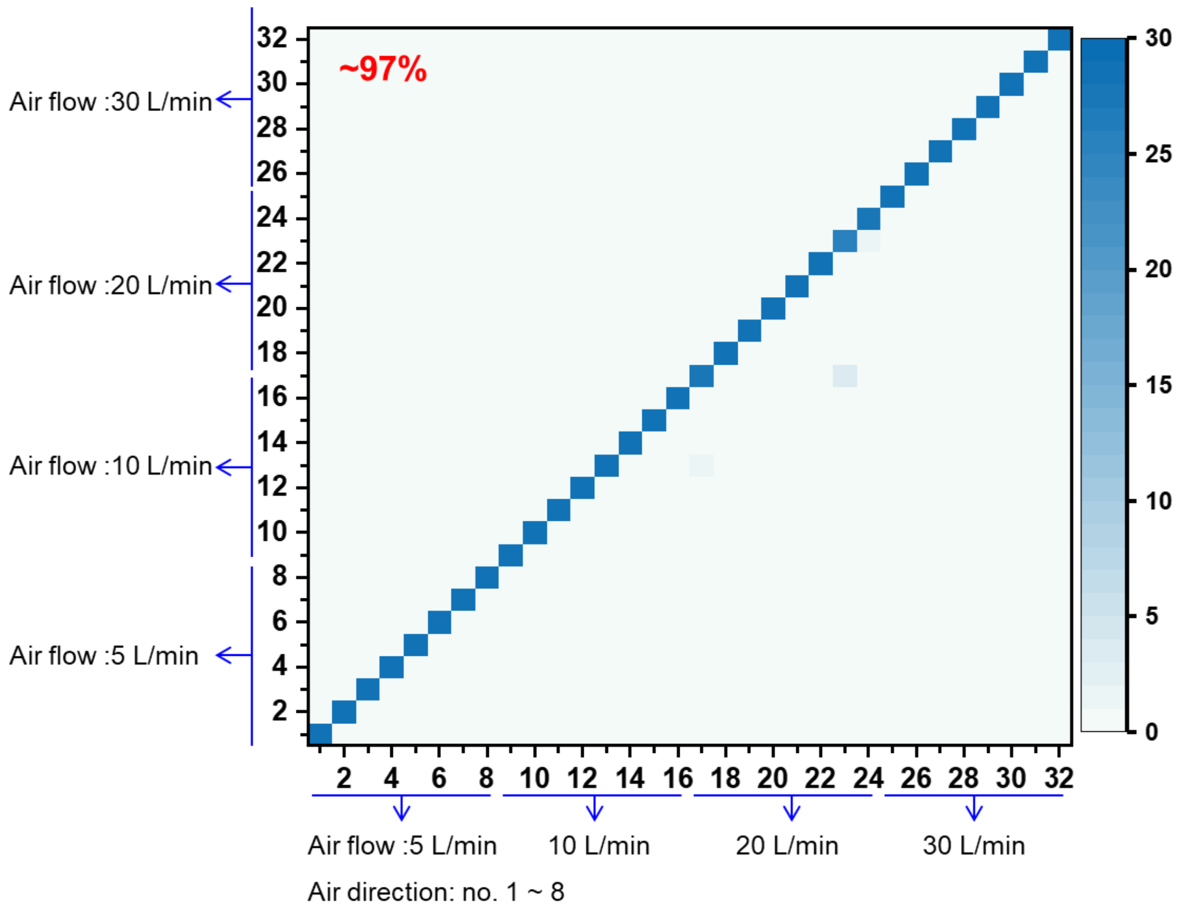

Figure S16. Multi-class classification performance for combined airflow rates and directions. The visualization shows the classification results for 32 total classes, formed by combining four airflow rates (5, 10, 20, and 30 L/min) with eight air directions (no. 1~8).